https://dx.doi.org/10.1016/j.buildenv.2023.110205

Evaluating a combined WRF and CityFFD method for calculating urban wind distributions

Jue Wang [a], Liangzhu (Leon) Wang [b], Ruoyu You [a]*

[a] Department of Building Environment and Energy Engineering, The Hong Kong Polytechnic University, Hong Kong Special Administrative Region of China

[b] Department of Building, Civil and Environmental Engineering, Concordia University, Montreal, Canada

* Corresponding author: ruoyu.you@polyu.edu.hk

Abstract

Inflow boundary conditions are critical for simulating urban wind fields by CFD methods, and wind profiles within the atmospheric boundary layer are significantly affected by local atmosphere circulation and diurnal variation. The Weather Research and Forecasting (WRF) model is a powerful mesoscale weather prediction model that can be used to provide more realistic inflow boundary conditions. To investigate the potential of a combined WRF and CityFFD method (WRF-CityFFD), this study first validated the WRF and CityFFD models and then used the validated models in WRF-CityFFD to calculate the wind distribution in the Kowloon district of Hong Kong within an area of 3.5 km × 2.4 km. The wind speed data at two weather stations were used as a benchmark, and CityFFD with inflow boundary conditions from a semi-empirical method (semi-empirical-CityFFD) was also investigated for comparison. The WRF-CityFFD performed better than the semi-empirical-CityFFD in calculating wind velocities in urban microclimates. The power-law exponent for wind profiles should be carefully defined when conducting CFD simulations for complex urban layouts. Coastal areas with onshore wind conditions were more suitable for selection as inflow boundary conditions for WRF-CityFFD.

Keywords

Urban wind distribution; Multiscale; Fast fluid dynamics; Power-law wind profile; Weather research and forecasting

1. Introduction

According to the Intergovernmental Panel on Climate Change (IPCC), more than half of the world's population presently lives in urban regions, and this number will rise to 70% by 2050 [1]. The urban wind distribution around buildings in the lower portion of the atmospheric boundary layer (ABL) plays

a significant role in the urban climatic system [2, 3]. The airflow over the roofs affects the interchange of pollutants and heat between the street canyon and the overlying ABL [4, 5]. Furthermore, the wind distribution within the street canyon is closely related to natural ventilation, pedestrian comfort, and pedestrians' exposure to pollutants [6, 7]. Therefore, it is crucial to better understand wind distributions at the urban scale.

Numerical simulation has become one of the most popular ways to investigate urban wind distributions. Computational fluid dynamics (CFD) has been widely utilized [4, 8-15], as it can fully model the topography and built-up areas of the target region. For instance, van Hoof et al. [14] established a complex geometry for a football stadium with a 500-m radius with detailed windows and steel roof constructions. They used CFD to calculate the wind flow around the stadium to study its natural ventilation. Toparlar et al. [15] explicitly modeled the buildings located in a circular area with a diameter of 1200 m to investigate the urban microclimate of the Bergpolder Zuid region in the Netherlands. Fast fluid dynamics (FFD) is a unique algorithm based on CFD, and the semi-Lagrangian approach is used for advection terms in the Navier-Stokes equations [16, 17]. Extensive validation efforts have demonstrated the accuracy and computing efficiency of the FFD approach [16-21]. Dai et al. [21] evaluated the performance of the traditional CFD and FFD for outdoor airflow and pollutant dispersion using experimental wind tunnel data as the benchmark. They found that the use of FFD with a proper turbulence model can reduce computing time without sacrificing accuracy. Therefore, FFD simulations have been used for urban wind modeling up to the scale of several kilometers. For example, Mortezazadeh et al. [22] developed a simulation tool named City Fast Fluid Dynamics (CityFFD), and they simulated the urban microclimate in a region of 3 km × 3 km.

For CFD modeling, setting inflow boundary conditions is critical for obtaining an appropriate flow field [2, 8]. The wind profile within the urban ABL features a power-law [25-27] or a log-law expression [23, 24]. Experimental studies have found that the log law does not adequately describe the wind speed profile above 200 m [25, 26], while the power law fits better [27]. The power-law profile has an exponent ranging from 0.1 to 0.5 [28, 29]. The power-law coefficient is normally determined empirically from the urban surfaces and topography as a constant for CFD inflow boundaries [30]. The wind speed at a reference height, such as the speed measured at a meteorological station, is also needed [12, 13]. Therefore, this method for setting the inflow boundary conditions is a semi-empirical method. However, it has been reported that the power-law exponents of the ABL can vary strongly with spatial and temporal factors [31-35]. He et al. [33] investigated the wind profiles in Hong Kong under typical summer conditions with Doppler LiDAR. They observed that wind profiles were significantly modified by urban layouts, and the power of the wind profile was much higher in built-up areas. Halios and Barlow [34] reported the morning transition of the ABL in London, attempting to explain the diurnal variation of the ABL's power-law value. Lim et al. [35] found that the power-law index for wind profiles was time-dependent in Tokyo due to the diurnal cycle, with higher values (0.2-0.3) at night and lower

values (0.1) during the daytime. Therefore, the semi-empirical methods for generating the inflow boundary conditions for CFD models, especially the wind profiles, are idealized and oversimplified.

To provide more realistic inflow boundary conditions for CFD simulations, mesoscale modeling is a potential solution, such as the Weather Research and Forecasting model (WRF) [36, 37]. Simulations with the WRF model are mainly conducted with spatial resolution from several hundred meters to several hundred kilometers. These grand spatial scale models can rationally reproduce meteorological phenomena, including diurnal variation, sea breezes, and heat waves [37]. Given the situation above, multiscale modeling has been proven to be a potential method for providing CFD models with more accurate inflow boundary conditions [38-41]. Tewari et al. [41] used WRF output data, including wind velocity components, turbulence kinetic energy (TKE), and potential temperature, as the initial and boundary conditions. They found that the accuracy of the CFD-Urban model has improved when using WRF output for pollutant propagation simulations, compared with using measured data as initial and boundary conditions. Mortezazadeh et al. [42] integrated CityFFD and WRF to investigate the urban temperature distribution during heat waves. They used WRF results such as the wind velocity at the height of 10 m, air temperature, and street surface temperature as input for the CityFFD simulation and found that it is important to use microclimate simulations to study urban heatwaves. However, there has been only limited research on the use of wind profiles obtained by mesoscale modeling for CFD models. Therefore, it is meaningful to evaluate the performance and applicability of the time-varying wind profiles obtained from mesoscale models.

The present study aimed to evaluate a combined WRF and CityFFD method (WRF-CityFFD) for calculating urban wind distributions. The WRF and CityFFD models were first validated by two sets of experimental data from field measurements and wind tunnel tests. The validated models were then employed in the WRF-CityFFD method to calculate the wind distribution in the Kowloon district of Hong Kong within an area of 3.5 km × 2.4 km. The wind speed data at two weather stations in the calculation domain was used as a benchmark to evaluate the combined method. For comparison, CityFFD with inflow boundary conditions from a semi-empirical method (semi-empirical-CityFFD) was also evaluated. Finally, this study discussed the applicability of the combined method.

2. Methodology

2.1. CityFFD

The CityFFD model solves the following continuity, momentum, and energy equations for incompressible flows [42]:

$$\nabla \cdot \mathbf{V} = 0 \tag{1}$$

$$\frac{\partial \mathbf{V}}{\partial t} + (\mathbf{V} \cdot \nabla)\mathbf{V} = -\nabla \mathrm{P} + \left(\frac{1}{Re} + v_t\right)\nabla^2 \mathbf{V} - \frac{Gr}{Re^2} T \tag{2}$$

$$\frac{\partial T}{\partial t} + (\mathbf{V} \cdot \nabla)T = \left(\frac{1}{Re \cdot Pr} + \vartheta_t\right)\nabla^2 T \tag{3}$$

where $\mathbf{V}$, T, P and t are the velocity, temperature, pressure and time, respectively; Re, Gr and Pr are the dimensionless Reynolds number, Grashof number, and Prandtl number, respectively; and v_t and ϑ_t are turbulence-related parameters, i.e., turbulent viscosity and turbulent thermal diffusivity.

CityFFD adopts the semi-Lagrangian method for the advection term in Eqs. (2) and (3). Therefore, no iteration is needed to calculate the velocity field, and computing costs are reduced [43]. The split scheme for the semi-Lagrangian method is shown in Eqs. (4) and (5) [17]:

$$\frac{\partial \emptyset}{\partial t} + (\mathbf{V} \cdot \nabla)\emptyset = \frac{d\emptyset}{dS} \tag{4}$$

$$S^n \approx S^{n+1} - \mathbf{V}\Delta \mathrm{t} \tag{5}$$

where $\emptyset$ refers to the velocity or temperature in Eqs. (2) and (3); and S represents the characteristic curve of the fluid particle, based on which S^n and S^{n+1} are the positions of the particle at times n and n+1, respectively. The detailed high-order interpolation scheme can be found in our previous work [16, 20, 44]. It has been proven that the applied 3rd-order backward and forward sweep interpolation scheme has an accuracy comparable to that of the 4th-order scheme and could significantly reduce the numerical errors and computing time when simulations are conducted with coarse grids and large time steps. A Poisson equation is used for updating pressure domains [20].

Large-eddy simulation (LES) was found to be potentially more accurate than Reynolds-averaged Navier–Stokes models for outdoor simulations [8]. Therefore, LES was adopted as the turbulence model in the present study. As CityFFD uses a high-order interpolation scheme, the Courant–Friedrichs–Lewy (CFL) number is recommended to be between 1 and 10 [22], and this study used 6.75. The turbulence viscosity is calculated as follows [45]:

$$v_t = (C_s \times l)^2 \left|\overline{S}\right| \tag{6}$$

where C_s is the Smagorinsky constant, typically between 0.1 and 0.24 [8], and equal to 0.18 in this study; l is the filter width; and $\overline{S}$ is the large-scale strain rate. For calculating the filter width l and strain rate $\overline{S}$, the following equations are used here [18]:

$$l = (\Delta x \Delta y \Delta z)^{1/3} \tag{7}$$

$$\overline{S} = \frac{1}{2}\left(\frac{\partial u_i}{\partial x_j} + \frac{\partial u_j}{\partial x_i}\right) \tag{8}$$

where $\Delta x, \Delta y, \Delta z$ are the discrete lengths in the x, y, and z directions, respectively. Meanwhile, the i-index indicates the x, y, and z directions.

2.2. Inflow boundary conditions for CityFFD

This section describes two methods applied in this study for generating inflow boundaries for the CFD models, the semi-empirical method (for semi-empirical-CityFFD) and the mesoscale modeling (for WRF-CityFFD). As the tallest building of the target complex urban area in this study was 284 m, both methods approximated the wind profile at the CFD inlet boundary as a power law. The semi-empirical method used the wind speed measured by the windward weather station nearest to the CFD domain and an empirical power-law coefficient. For the combined method of CFD and mesoscale modeling, both the wind speed and the power-law coefficient at the inlet boundary were extracted from WRF simulations in this study.

2.2.1. Semi-empirical method

The wind profile was approximated as a power law, as shown in Eq. (9) [2].

$$U(z) = U_{ref}\left(\frac{z}{z_{ref}}\right)^{\alpha} \tag{9}$$

where $U(z)$ is the wind velocity $(\mathrm{m/s})$ at the height of z, U_{ref} is the velocity $(\mathrm{m/s})$ at a reference height z_{ref} (m), and α is the power-law coefficient. In this method, U_{ref} was determined by the windward weather station closest to the CFD domain, and z_{ref} was the height of the wind-measurement point at the station. Meanwhile, α was selected in accordance with the terrain category and the roughness. According to previous studies, as the land surface changes from smooth (e.g., sea) to rough (e.g., downtown areas), the value of α gradually increases from 0.1 to 0.5 [28, 29].

2.2.2. From mesoscale modelling: WRF

In the mesoscale modeling method, the WRF model was used for calculating meteorological conditions, as shown in Fig. 1. The WRF model is a powerful mesoscale numerical weather prediction system consisting of advanced physics schemes and multi-physics parameterizations for modeling major atmosphere processes with grid spacing from hundreds of meters to hundreds of kilometers [35, 37, 46]. For the land surface, planetary boundary layer, atmospheric and surface radiation, microphysics, and cumulus convection, WRF offers various physics options that have been thoroughly proven in previous research [47]. To obtain the wind profile at the inflow boundary, U_{ref}, z_{ref}, and α were all extracted from WRF results. As this work focuses on urban wind fields, the wind profiles in the bottom portion of the ABL, below a height of 350 m, were utilized to obtain α. η in the flow chart represents the vertical layer used in the WRF model, and it was established according to the pressure gradient [55].

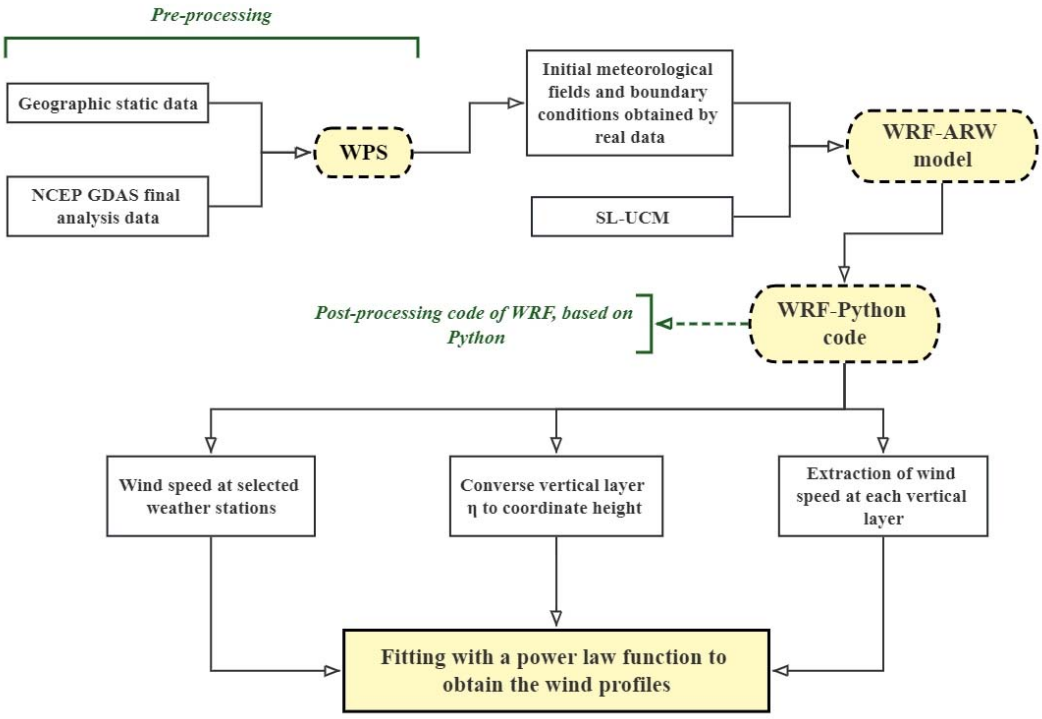

Fig. 1. Flowchart to obtain inflow boundary conditions from WRF simulation.

To rationally reproduce the meteorological phenomena, the selected physical parameterization for WRF is summarized in Table 1. In this study, the initial and lateral boundary conditions to force the WRF simulation were obtained from the NCEP GDAS final analysis with 0.25-degree horizontal resolution

and 6-h temporal resolution [48]. The Noah land surface model (LSM) provides surface sensible and latent heat flux as well as skin temperature as the lower boundary [49], and the urban canopy model (UCM) provides the urban friction based on the land cover/land use at the sub-grid scale. This study used the integrated model (SL-UCM) to determine the momentum fluxes of the urban canopy [50]. When these basic models are integrated into the WRF, the outputs can be directly adapted to the CityFFD model.

Table 1. Physical parameterization of the WRF model.

Category	Description
Planetary boundary layer scheme	Mellor-Yamada-Janjic scheme [46, 51]
Microphysics	Lin scheme [47, 52]
Cumulus parameterization	Grell-Devenyi ensemble schemes [48, 53]
Shortwave and longwave radiation	RRTM [49, 54]
Land surface model	Noah [44]
Urban canopy model	SL-UCM [45]
Advection scheme	Runge–Kutta 3rd order

3. Model validation

3.1. Mesoscale modelling: WRF

To validate the mesoscale model, we chose the Kowloon peninsula domain as the WRF study domain, as shown in Fig. 2(a). We used WRFv4.0 to calculate the meteorological conditions, and the wind speed measured by the four weather stations in our study area was employed as the benchmark. Star Ferry (SF) and Shell Oil Depot (SOD) were located near the coastal areas, while the Hong Kong Observatory (HKO) and King's Park (KP) were situated in the downtown areas and surrounded by high-rise buildings (see Fig. 2(a)). The exact geographical locations of the weather stations are summarized in Table 2. As shown in Fig. 2(b), three-nested domains were configured for WRF calculation using grid spacings of 1.8 km (113×128 grid points), 0.6 km (127×148 grid points), and 0.2 km (112×112 grid points) for a parent domain (d01) and two nested domains (d02, d03), respectively. A two-way coupling strategy [55] was adopted for the adjacent domains. A total of 34 sigma vertical levels were used for all domains, and 13 of the layers were under 1 km in height. Three typical calm wind days (from 08:00 on 19 October to 14:00 on 22 October 2016) were simulated to represent typical wind conditions in Hong Kong. The mean daily wind speed during selected simulation period was 2.95 m/s, 3.70 m/s and 9.04 m/s, respectively. According to the Hong Kong Observatory, the mean daily wind speed in Hong Kong ranges from 2 m/s to 10 m/s. Therefore the chosen days are typical in Hong Kong. The first 26 hours were taken as the spin-up period. WRF results were recorded every 20 min.

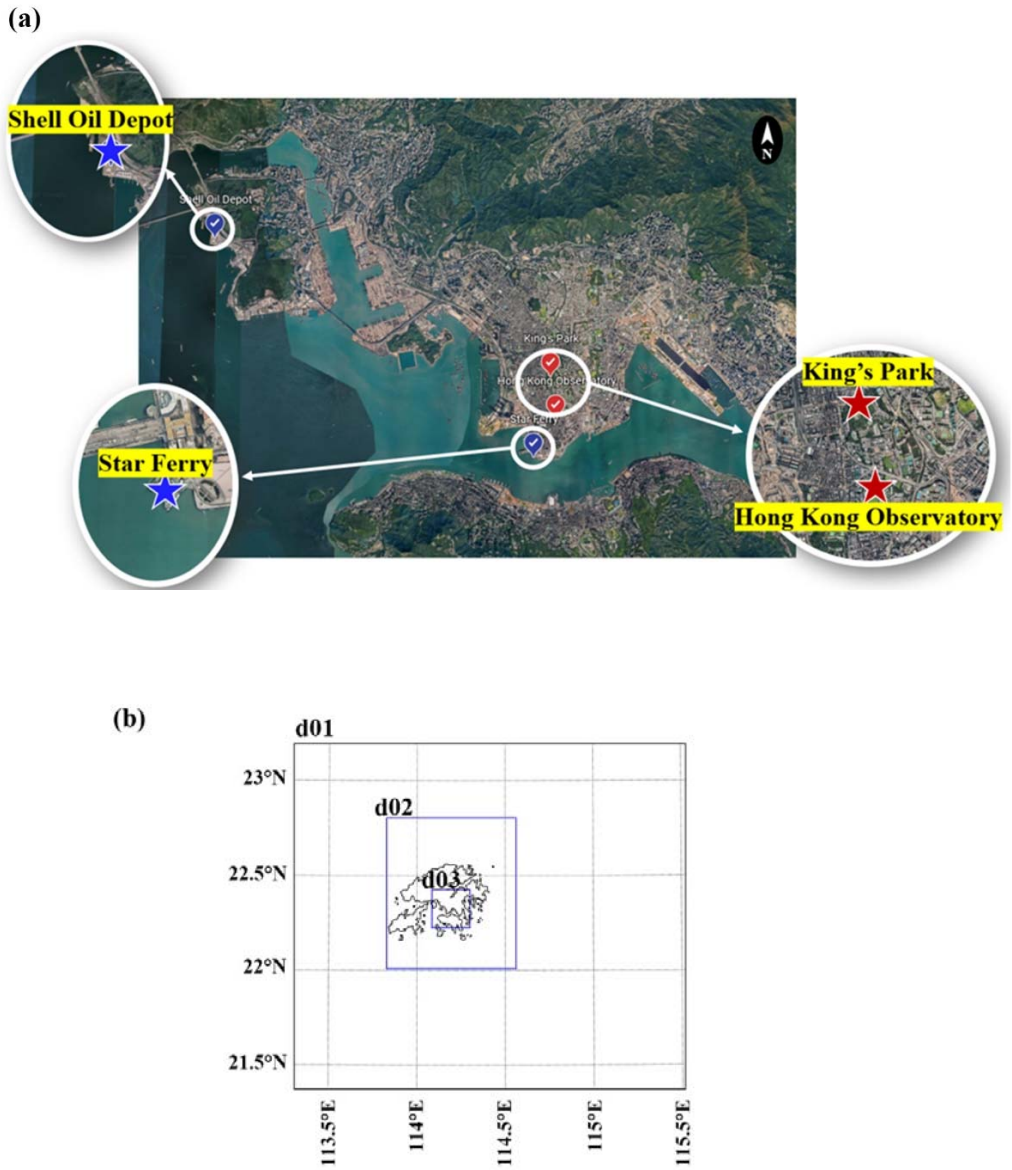

Fig. 2. (a) Four weather stations located in the innermost domain and (b) domain setup of the WRF

Wind measurement data with a temporal resolution of 1 min was available from local authorities. The most recent 20-min averaged wind speed was used to represent the wind speed at this time point. For instance, the wind speed at 10:00 was calculated as the average wind speed from 09:40 to 09:59. Fig. 3 compares the measured wind speed and the WRF-simulated results over time for the four weather stations. The simulation results at all four stations captured the trend in the wind speed as it gradually increased from 20 October to 21 October and then decreased. The simulated results exhibited the best agreement with the measured data at the SF station. However, WRF significantly overpredicted the wind speed for HKO and KP during the period from 23:20 on 20 October to 00:20 on 22 October. The

largest discrepancies were 8.24 m/s and 10.66 m/s for HKO and KP, respectively, occurring at 08:20 and 09:00, respectively, on 21 October. As shown in Fig. 3, the measured wind speed in the downtown area (HKO and KP) was relatively stable compared with that in the upstream station (SF). This phenomenon may be attributed to the complexity of the urban layouts, especially associated with the high-rise buildings in Kowloon, and it is consistent with the field test by He et al., [33]. However, in WRF simulations, the urban canopy was parameterized by the drag force with the specific value of building height of 10 m [50]. A high consistency of simulated wind speed can be found at the upstream station (SF) and downtown stations (HKO and KP). Therefore, the discrepancies between measured data and simulated results could be caused by the urban canopy model used in WRF.

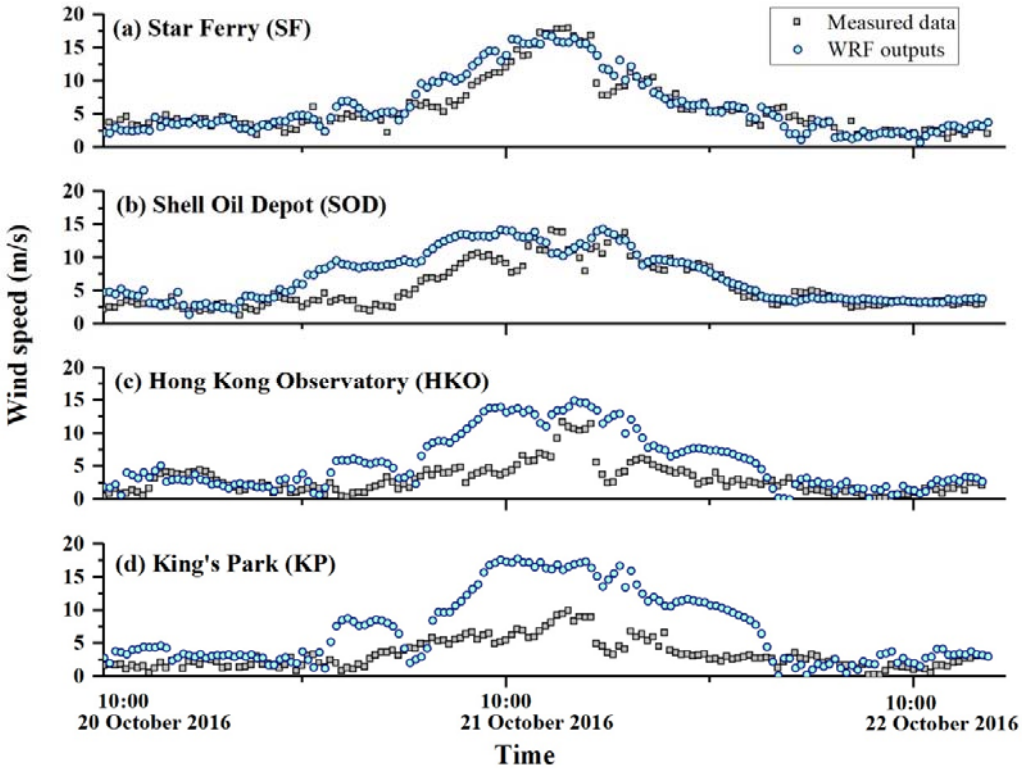

Fig. 3. Comparison of measured wind speed and WRF-simulated results over time for the four weather stations: (a) SF, (b) SOD, (c) HKO, and (d) KP.

To quantitatively analyze the performance of the mesoscale model, the mean bias error and the root mean square error were prevalently used [38, 41]. Thus, these two parameters were calculated in this work to evaluate the performance of WRF simulations. The mean bias error (MBE) assesses whether the simulated wind velocity is overestimated or underestimated compared to the measured values (see

Eq. (10)). The root mean square error (RMSE) is widely used to indicate the deviation of the simulated results (see Eq. (11)).

$$\mathrm{MBE} = \frac{\sum_{i=1}^{n}\left(U_i^S - U_i^M\right)}{n} \tag{10}$$

$$\mathrm{RMSE} = \sqrt{\frac{\sum_{i=1}^{n}\left(U_i^S - U_i^M\right)^2}{n}} \tag{11}$$

where U_i^S and U_i^M are the simulated and measured wind velocity, and n is the number of measured data points for one sampling location. In this study, n was 158. As summarized in Table 2, WRF exhibited the best performance at SF and the worst at HKO. The MBE and RMSE for SF were 0.58 m/s and 1.79 m/s, respectively, and those for HKO were 3.89 m/s and 5.49 m/s, respectively. Wong et al. [40] recently compared WRF results with measured data for five locations on a university campus in Singapore. The MBE in their study ranged from 2.58 to 3.90 m/s, and the RMSE from 2.69 to 4.13 m/s. Thus, our WRF results showed similar accuracy to those in the literature for dense urban areas.

Table 2. Geographical locations, MBE and RMSE at each weather station.

Station Name	Star Ferry (SF)	Shell Oil Depot (SOD)	Hong Kong Observatory (HKO)	King's Park (KP)
Position	Coastal	Coastal	Downtown	Downtown
Latitude (°N)	22.29	22.34	22.30	22.31
Longitude (°E)	114.17	114.08	114.17	114.17
Elevation (m)	18	43	32	65
MBE (m/s)	0.58	1.67	3.89	2.68
RMSE (m/s)	1.79	2.75	5.49	3.95

3.2. CityFFD

A wind tunnel experiment for the Japanese city of Niigata conducted by Tominaga et al. [56] was used for CityFFD validation, as described in this section. The tallest structure was 60 m high in full scale, and the radius of the urban building geometries was 500 m, as shown in Fig 4(a). The experiment measured the time-averaged wind speed at 80 sampling points, as shown in Fig. 4(b) [56]. All the sampling points were located at the height of 8 mm above the ground in the downscaled model, which corresponded to 2 m in full scale. Three sets of grid were tested with the total the cell number of 3.9 million, 19.4 million, and 40.4 million, and the grid with 19.4 million cells was sufficient for this case. Structured grids were used in this model, as shown in Fig. 4(c), and uniform grids were distributed near the zone in which the buildings were situated, with dimensions of 1 m horizontally and 0.5 m vertically.

The total grid number was 19.4 million. The ground surface and building walls were set as non-slip conditions with smooth surfaces. Currently, CityFFD does not include wall functions, as our previous validation studies at the urban scale demonstrated acceptable accuracy for the outer layers and regions away from the surface without these functions [18, 57]. Additionally, for large urban scale simulations, the Y+ values are typically high, so a wall function may be beneficial in enhancing accuracy. This is a limitation of the current version of CityFFD, and we intend to implement wall functions to improve the simulation near surfaces. The downstream boundary was set as the pressure outlet, and the top and lateral boundaries were set to be symmetric. The inflow boundary condition was set as the measured results from the original study [56].

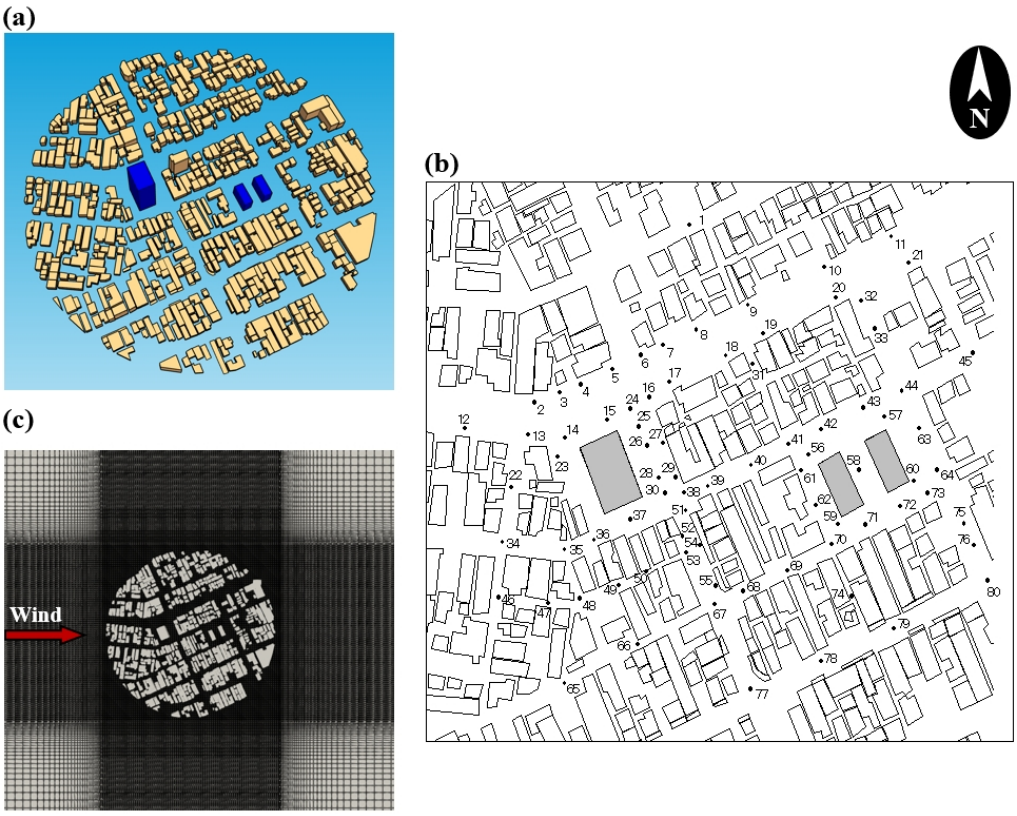

Fig. 4. (a) Geometrical models of the urban area used for validation, (b) positions of the sampling points in the wind tunnel experiment [56], and (c) mesh design for the simulation.

Fig. 5 compares the measured results, the simulated results in this study, and the CFD results reported by Tominaga et al. [56]. The wind speed ratio was defined as the ratio between the wind speed at each measuring location and that at the inflow border at the same height. For CFD simulations , mean relative errors are more widely used to evaluate the simulation performance [11, 12, 14]. Thus, using this parameter made it easier to compare our simulation performance with previous work. The mean relative

error of our calculation was -30.25% for the wind speed ratio, and the mean relative error for the same case in the literature [56] was -29.28%. The relative error of the CityFFD simulation was within acceptable limits based on previous studies on urban wind fields [12]. Therefore, our CityFFD results showed similar accuracy to that in the literature on an urban layout.

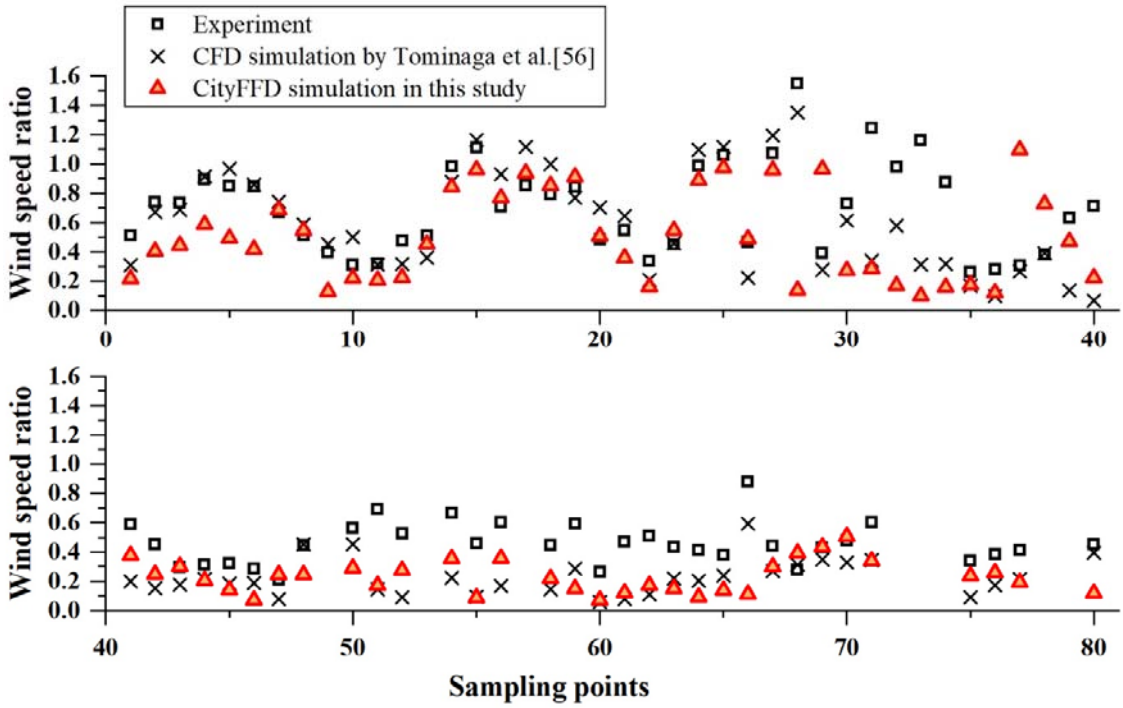

Fig. 5. Comparisons of the measured wind speed ratio and calculated results

4. Case setup

The Kowloon district in Hong Kong was selected for evaluation of the performance and applicability of the time-varying power-law wind profiles obtained from mesoscale models. Kowloon, one of the first few areas to be developed in Hong Kong, has an extremely complex and dense urban morphology [58]. During the time period between 16:00 and 24:00 on 21 October 2016, the wind direction was stable at the southeast. Therefore, CFD inflow boundary can be set at the same locaton, and this time period was chosen for the CityFFD simulation.

4.1. Computational domain and mesh design

According to the meteorological data, the wind direction for the Kowloon district during the calculation period was southeast (i.e., the wind-from direction was between 180° and 270°). Therefore, a domain

of 3.5 km by 2.4 km in the Kowloon Peninsula, as shown in Fig. 6(a), was chosen for this study. The weather station SF was in the windward direction, so the boundary of the study domain was set near SF. Fig. 6(b) shows the three-dimensional geometric model of the selected area. Note that all buildings and terrain were explicitly resolved in this model; other obstacles, such as greenery and roads, were neglected. The geometric data was transformed from public sources such as OpenStreetMap, NASA, and USGS [59]. An et al. [10] recommended the inclusion of buffer areas for geometric models with topography. These areas should ideally be sloped at an inclination angle (θ) of less than 30° in order to minimize the impact of an elevated terrain border on the simulation results. Therefore, buffer areas indicated by the dark grey shading in Fig. 6(b) and (c) with θ of 20° were included in the geometric model. This is also the reason that SF was set near the geometric boundary rather than at the boundary. Two meteorological stations, KP and HKO, were located in the study area, and their measured data were used as a benchmark.

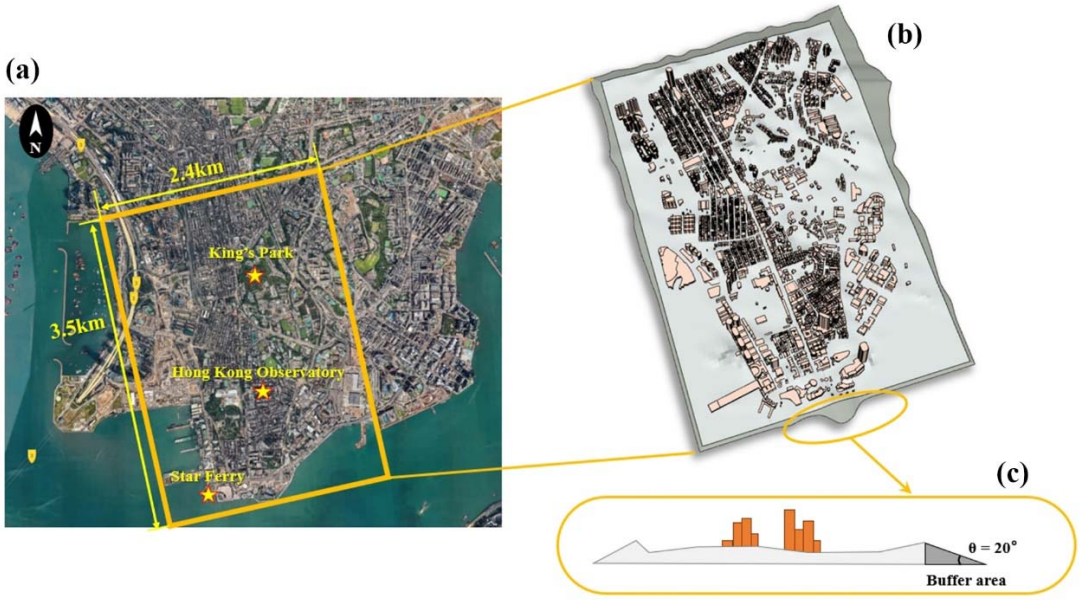

Fig. 6. Study area for CityFFD simulation: (a) plane view of the target area (where weather stations are marked with stars), (b) geometries of buildings and terrain, (c) setting of buffer areas.

This study followed the recommendations of AIJ [29], COST guidelines [60], and An et al. [10] to determine the computational domain size for CityFFD simulation. The vertical length of the computational domain should be no less than $5H_{max}$, where H_{max} is the height of the tallest building within the target area. The lateral boundaries of $5H_{max}$ are recommended. Meanwhile, the blockage ratio should be less than 3%, and artificial acceleration should not be observed near the borders. In this case, the tallest structure located in the study area was 284 m high (H_{max}), so the whole model was 5.30 km long, 5.08 km wide, and 1.45 km high (see Fig. 7(a)). Note that the lateral boundaries in the

downstream area were $4H_{max}$, due to the limitations of computing capacity. The blockage ratio was 1%, and no artificial acceleration was observed.

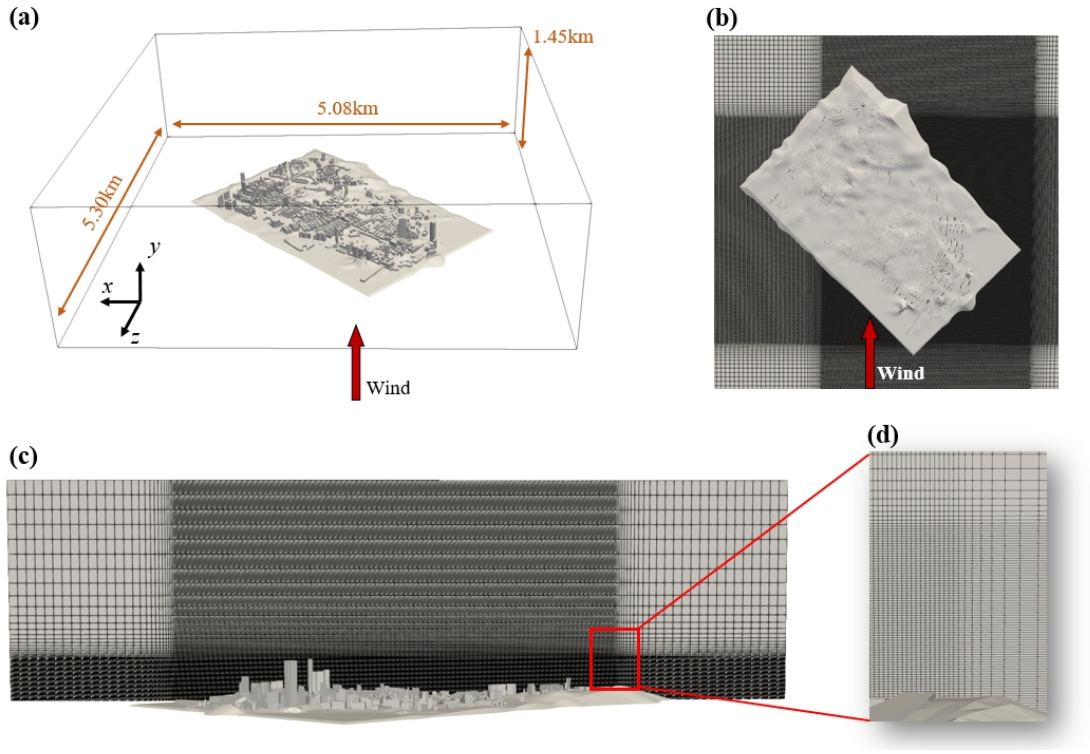

Fig. 7. Setup of CityFFD simulations: (a) computational domain, (b) mesh design in the horizontal direction and (c) vertical direction, (d) details of the grid transition section.

The mesh generation techniques of the CityFFD simulation were based on the staggered Cartesian meshes, and more information about this technique can be found in our previous work [22, 61]. Three sets of grid were tested with the grid number of 35.3 million, 105.6 million, and 229.4 million, and the 105.6 million grids were chosen after the grid independence test. The details of the mesh design are shown in Fig. 7(b-d). The grid size near buildings and terrain was 4 m horizontally and 2 m vertically, which satisfied the grid size requirement [22]. The grid size gradually increased to 60 m in all directions at a stretching ratio of 1.2. The total grid number was 105.6 million. The numerical simulations were conducted by a PC with GPU NVIDIA GeForce RTX 3080, and the computing time for each case was 10 h.

4.2. Inflow boundary conditions

The wind during the simulated duration was sweeping from the southeast across the calm sea surface. Thus, the transition area upstream of the study domain was assumed to have no effect on the approach wind. Based on the assumptions, this study used the wind profile at SF as the inflow boundary condition. The inflow boundary was set as the velocity inlet, and this study approximated the wind profile at the inlet as a power law following Eq. (9). The obtained U_{ref}, α, and z_{ref} for the inflow wind profile in the two methods are described below.

4.2.1. Semi-empirical method

In the semi-empirical method, the measured wind speed and direction at SF were used for the inflow boundary conditions. The power-law coefficient α in this method was set as 0.18 [10], and z_{ref} for SF was 18 m above sea level. The measured wind speeds at SF (Fig. 3(a)) were used as U_{ref}.

4.2.2. From mesoscale modelling: WRF

Similarly, the WRF-calculated wind profile at SF was used for the inflow boundary conditions in this method. The WRF case setup was the same as that for the WRF validation case in Section 3.1. The innermost domain of WRF contained the built-up areas in Kowloon and covered the CityFFD simulated area. The calculated SF wind profile was obtained from data at the grid point closest to SF. Note that the WRF model has a horizontal grid resolution of 200 m in that region; thus, SF and the windward boundary of the study domain were in the same element. The power-law coefficient α and U_{ref} were obtained for 22.29 °N and 114.17 °E, and z_{ref} for SF was 18 m above sea level. Unsteady simulation was conducted for WRF simulation, and the results were extracted with an interval of 20 min. The calculated wind speeds at SF can be found in Fig. 3(a).

Fig. 8 compares the time-varying power-law coefficient α from WRF simulation and the empirical value within the calculation period. The calculated power-law values of wind profiles from WRF varied between 0.133 and 0.359, and the empirically determined power-law value was within this range. In addition, the calculated power-law value was lower than the empirical value (0.18) in the afternoon (before sunset at 18:00), while it rose over 0.18 in the evening (after sunset). The calculated power-law coefficient then dropped slightly during the night. Thus, the local atmospheric circulation and diurnal variations can lead to changes in the power-law coefficients.

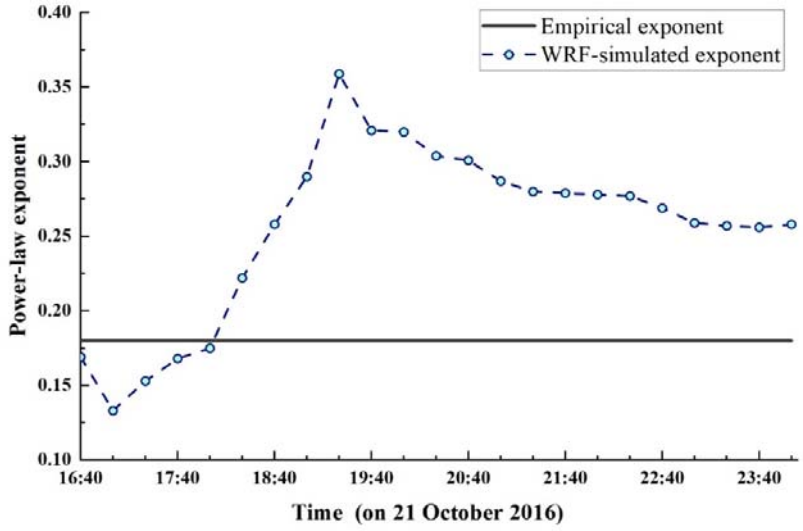

Fig. 8. Variation of the extracted power-law coefficient α during the simulation period on 21 October 2016.

5. Results and discussion

To evaluate the combined method, we compared the simulated wind speeds from WRF-CityFFD and semi-empirical-CityFFD with the measured wind speeds at KP and HKO as the benchmark. We further compared the two methods in calculating flow distributions at the height of the two stations. Finally, we assessed the WRF prediction capacity at different weather stations to explore the applicability of the combined method.

5.1. Comparison between WRF-CityFFD and semi-empirical-CityFFD

The comparisons of WRF-CityFFD and semi-empirical-CityFFD with the measured data at KP and HKO are shown in Fig. 9(a) and (b), respectively. The results of WRF-CityFFD were mostly comparable with the measured values, while those of the semi-empirical-CityFFD significantly deviated from the measured data at some time points. For example, at 19:40 for KP, the wind speed obtained by WRF-CityFFD was 4.12 m/s, comparable with the monitored data (3.54 m/s). In contrast, the result from semi-empirical-CityFFD was 6.97 m/s, and it was 96.9% higher than the benchmark. For HKO, the measured wind speed at 17:00 was 5.51 m/s. Compared with the measured result, WRF-CityFFD predicted a similar speed of 5.35 m/s, while that from semi-empirical-CityFFD (7.96 m/s) was significantly higher. Therefore, WRF-CityFFD performed better than semi-empirical-CityFFD in calculating wind velocities in urban microclimates. Note that the inflow boundary condition of City-

FFD simulations were determined by both α and wind speed at SF station (U_{ref}) as in Eq. (9). Therefore, the simulated wind speed variation trend between the two methods was not necessarily the same as that of α in Fig. 8.

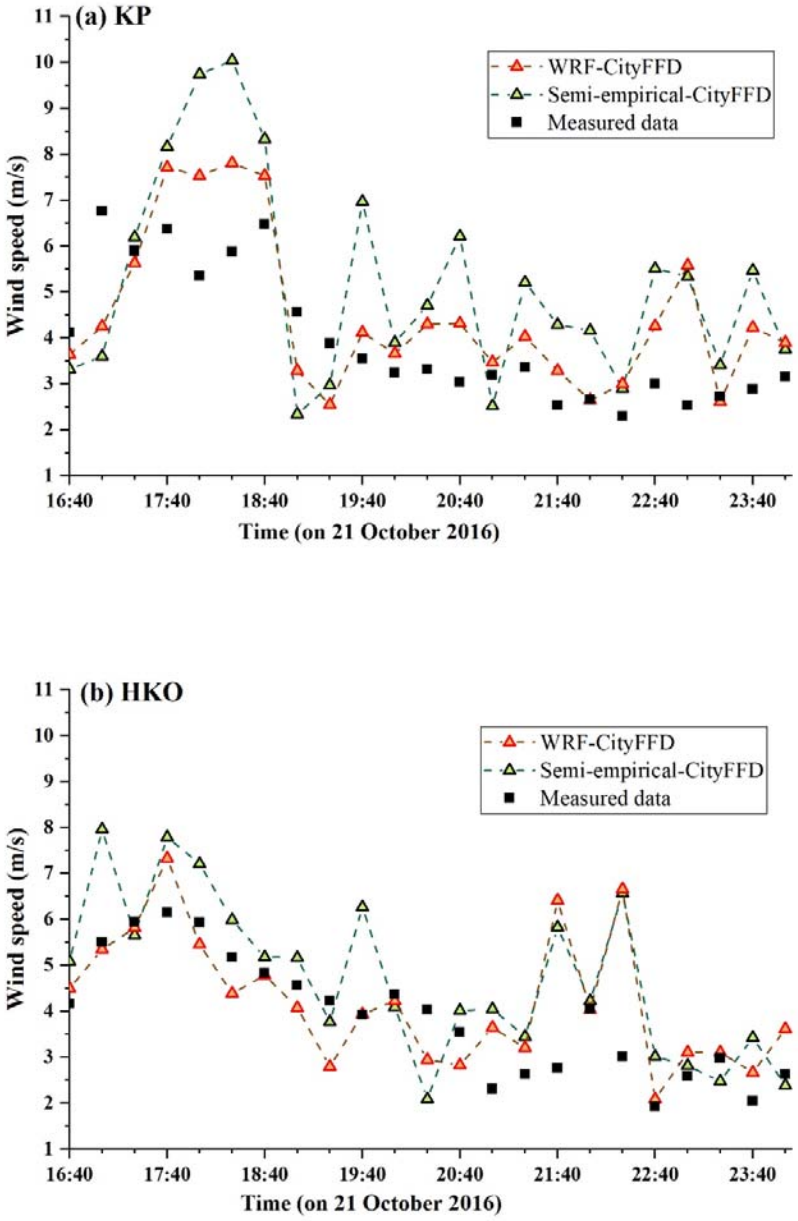

Fig. 9. Comparisons of the semi-empirical-CityFFD results and WRF-CityFFD results with the wind speed measured at (a) KP and (b) HKO on 21 October 2016.

For a quantitative assessment of the performance of the two methods, Table 3 shows the relative deviation, MBE, and RMSE for the two methods at KP and HKO. The relative deviation of WRF-

CityFFD was 18.1% at KP and 14.7% at HKO, and the relative deviations of semi-empirical-CityFFD were 37.2% and 26.1% at KP and HKO, respectively. The MBE and RMSE of the WRF-CityFFD results were also lower than those of the semi-empirical-CityFFD results at both stations. In addition, previous studies have used semi-empirical inflow boundary conditions for CFD modeling to calculate airflows for actual urban layouts. The relative error of their numerical simulations ranged from 20.0% to 40.8% when compared with the measured wind speed in field tests [8, 12, 13], which was higher than the relative deviation for the combined method in this study. For instance, Liu et al. [12] established a detailed full-scale model from a university campus to its nearest weather station, and their CFD model overestimated the wind velocity by 20%. Therefore, WRF-CityFFD has greater potential than the traditional CFD methods for accurately predicting urban wind distributions.

Table 3. MBE and RMSE of wind speed at KP and HKO.

Station name	KP		HKO	
Method	WRF-CityFFD	Semi-empirical-CityFFD	WRF-CityFFD	Semi-empirical-CityFFD
Relative deviation	18.1%	37.2%	14.7%	26.1%
MBE (m/s)	0.55	1.23	0.34	0.84
RMSE (m/s)	1.31	2.24	1.26	1.50

Next, we compared the wind fields calculated by WRF-CityFFD and semi-empirical-CityFFD at the height of the measuring points of HKO and KP. Fig. 10(a) and (b) compare the wind speed distribution at HKO calculated by the two methods at 17:00. In general, the obtained wind speed distributions were similar, while significant discrepancy was observed in the marked area. At this time point, the WRF-simulated α (0.133) at SF was lower than the empirical coefficient (0.18); thus, semi-empirical-CityFFD underpredicted the approach wind speed by 0.7 m/s compared with WRF-CityFFD. In contrast, in the marked area in Fig. 10(c), semi-empirical-CityFFD underestimated the wind speed by up to 4.6 m/s. Similarly, Fig. 10(d-f) shows the results at 19:20, and the WRF-simulated α (0.359) was larger than the empirical coefficient at that time. Compared with WRF-CityFFD, semi-empirical-CityFFD overestimated the approach wind speed by 0.2 m/s and the wind speed in the marked area by up to 4.2 m/s. Note that the average height of the building complex on the left side of the marked area was 50 m, and that of the building structure on the right side (represented by dashed polygons) was 23 m. Therefore, the marked area was in the wake region of the taller building complex in this study. The results show that the difference in the inflow boundary was exacerbated in the wake region. A similar phenomenon was observed at the height of KP. Moreover, the selected plane was above the rooftop of the lower construction in the marked area. Previous experimental studies found that ambient wind over rooftop level was correlated with pollutant dispersion within the street canyon [4, 5, 62, 63]. Considering that

urban areas have large numbers of high-rise buildings, especially in high-density cities, inflow boundary conditions could have a significant impact on the pollutant dispersion in street canyons within the wake regions. Therefore, the power-law exponent for wind profiles should be carefully defined when conducting CFD simulations for complex urban layouts.

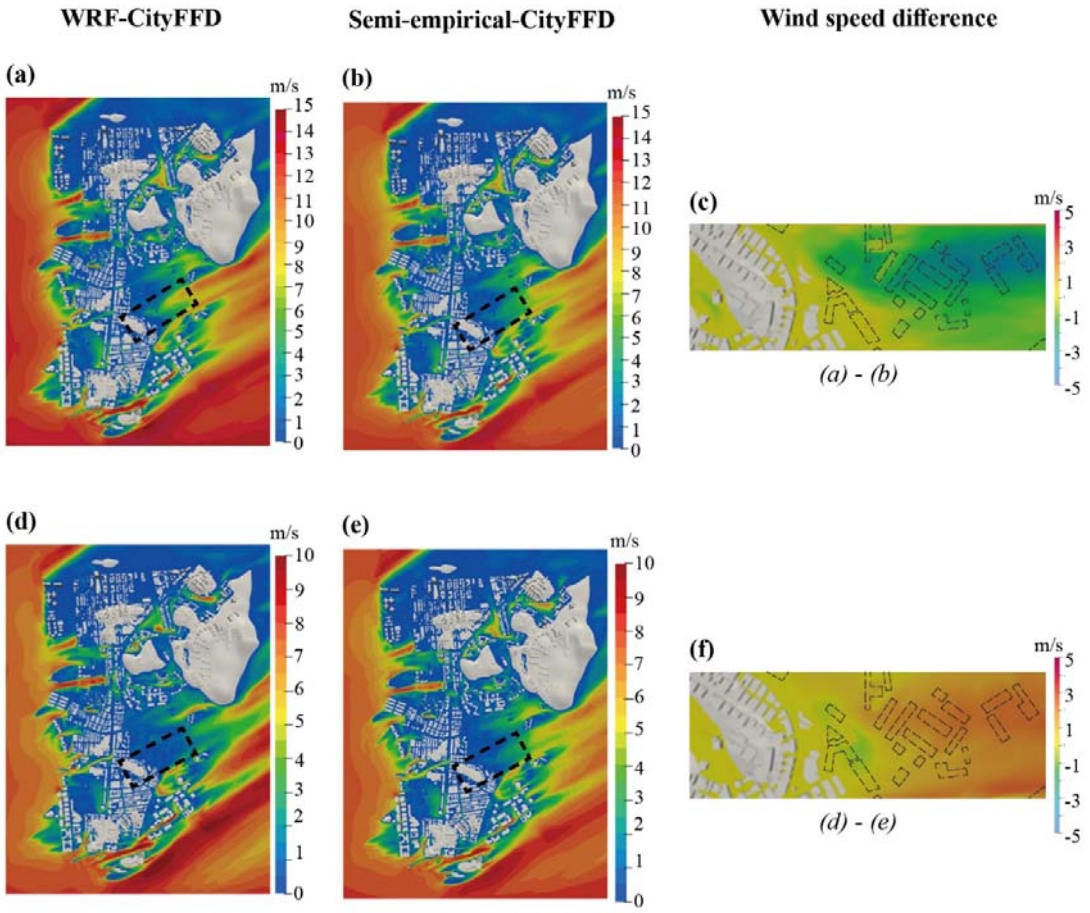

Fig. 10. Comparisons of the performance of the two methods at the height of HKO: When WRF-simulated α was lower than 0.18, and wind flow field was calculated by (a) WRF-CityFFD and (b) semi-empirical-CityFFD; and (c) the difference between the two. When WRF-simulated α was larger than 0.18, and wind flow field was calculated by (d) WRF-CityFFD and (e) semi-empirical-CityFFD; and (f) the difference between the two.

5.2. Applicability of the combined method

To assess the applicability of the combined method, we evaluated the WRF prediction capacity at different weather stations. Fig. 11 compares the WRF-simulated wind speed (horizontal axis) with the measured data (vertical axis) at each weather station. The solid line represents the 1:1 line, while the

dashed line is the relative error of ±30%. If a point is above the 1:1 line, the WRF overpredicted the wind speed compared to the measured data, whereas a point below the 1:1 line indicates an underprediction. The results show that at the coastal weather stations (SF and SOD), most of the points were within the range of ±30% relative error. However, at the downtown weather stations (KP and HKO), wind speeds were overestimated by more than 30% most of the time, especially when the measured wind speed was greater than 2 m/s. Therefore, the WRF performed better in the coastal area than in the downtown area. The specific value of building height in industrial and commercial areas was 10 m in SL-UCM [50] for WRF, while the tallest building of the target complex urban area in this study was 284 m. Thus, the default urban canopy parameterization schemes of SL-UCM could not represent urban morphology for high-density cities. Therefore, coastal areas were more suitable for selection as inflow boundary conditions for WRF-CityFFD. Similarly, for the inland cities, it is recommended that the borders of the built-up areas (for example, sub-urban or open and flat areas) be used as the inflow boundary conditions for WRF-CityFFD.

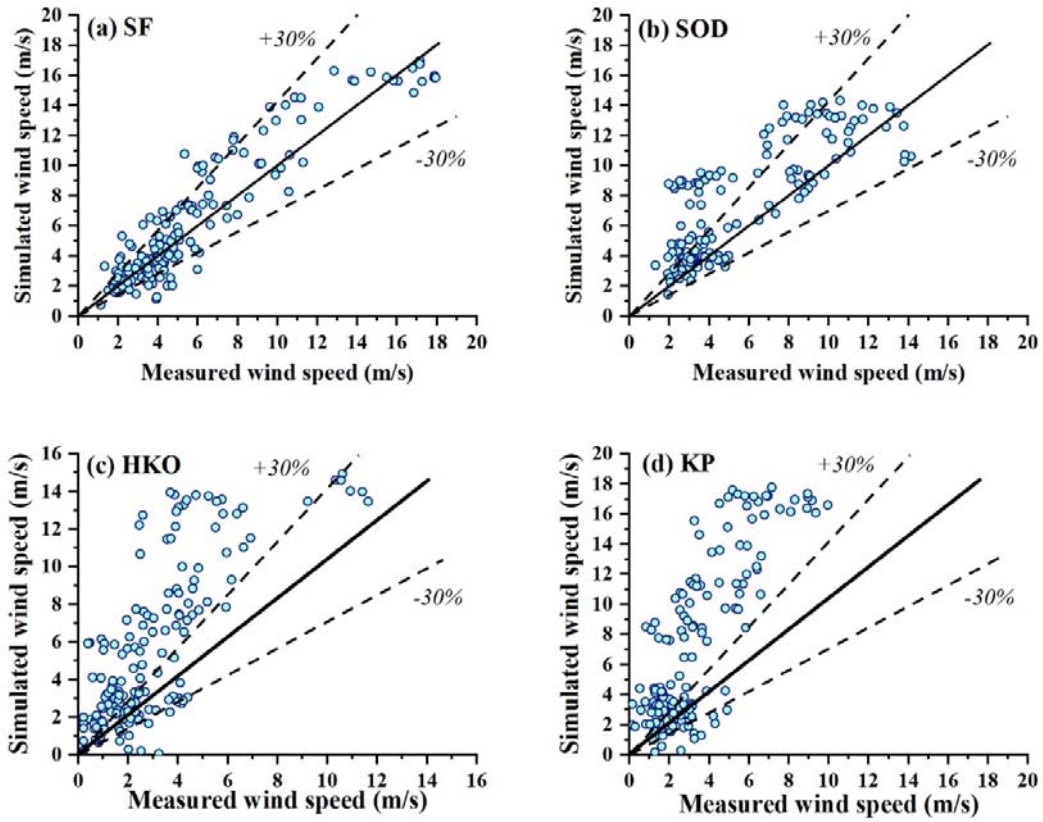

Fig. 11. Comparison of the WRF-simulated results and measured results at (a) SF, (b) SOD, (c) HKO and (d) KP.

We then compared the WRF-simulated wind speed under onshore and offshore wind conditions. The wind blew from the urban area to the SOD (offshore wind) during 26% of the simulation time; during the other 74% of the time, the wind swept across the sea (onshore wind). For SF, onshore wind occurred during 95% of the simulation time. Therefore, we only compared the simulated wind speed and measured wind speed at SOD under onshore and offshore wind conditions. As shown in Fig. 12(a), most of the time, WRF overpredicted the wind speed by over 30% under offshore wind conditions. Fig. 12(b) shows that WRF provided reasonably accurate predictions under onshore wind conditions for SOD. Thus, for coastal areas, onshore wind conditions are more suitable for use as inflow boundary conditions for WRF-CityFFD. For inland cities, the recommended scenario is an open area with few structures in the upstream direction.

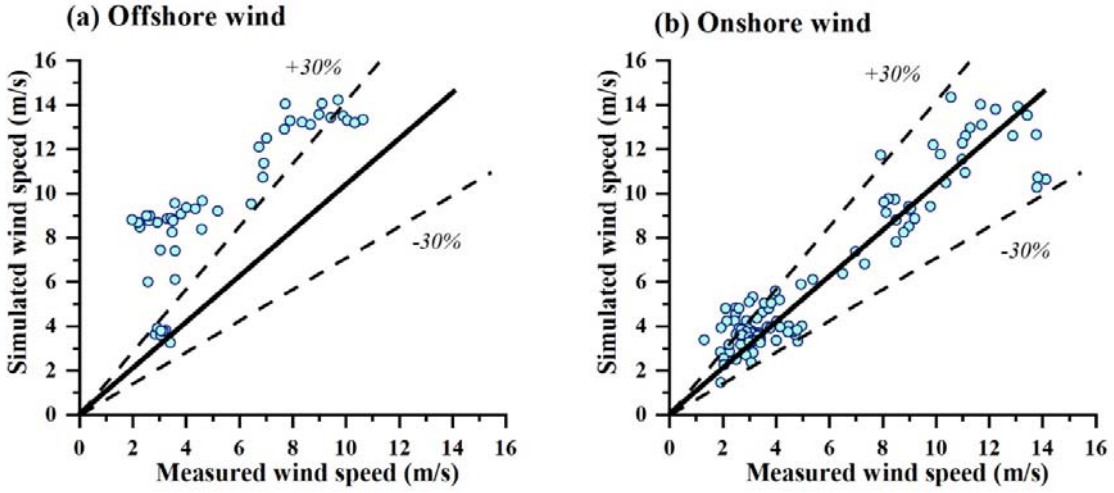

Fig. 12. Comparison of the WRF-simulated results and measured results under (a) onshore wind conditions and (b) offshore wind conditions at SOD.

6. Discussion

Note that the lateral length of the inflow was 5.08 km, which was larger than the horizontal grid resolution of the WRF (200 m). Taking 24:00 on 21 October 2016 as an example, the lateral wind speed ranged from 5.76 m/s to 6.98 m/s. However, only the wind conditions at the SF station were used in this study, and the lateral wind speed difference was not considered. The usage of WRF results along horizontal directions needs to be further evaluated for our future work. In this study, roads, and greenery were not taken into account using ground roughness. It was because our previous work has shown that the CityFFD with the setting of non-slip boundary conditions can provide reasonable results in both

wind-tunnel validation cases and full-scale urban simulations [18, 22]. However, future studies are needed to consider this aspect.

The combined WRF-CityFFD method can be used to calculate wind profiles flexibly and accurately, especially for cities with only a limited number of meteorological stations. The proposed combined method can help improve the model's ability to reproduce urban wind patterns. Thus, the method can be further used to provide the high-resolution wind microclimate, modeling down to the scale of the pedestrian level. Additionally, urban airflow plays an important role in removing and diluting pollutants. The mass exchange occurred both in the open space (directly blown away) and the layer above the urban canopy (pollutant removal due to turbulent fluctuations) in an urban atmosphere. Thus, accurate calculation of the urban wind distributions will be crucial for studies on the pollutant's transportation in urban areas, including dispersion in far fields and street canyons. Accordingly, the pollutants exposure for urban residents can be further investigated.

7. Conclusions

This investigation aimed to evaluate the potential of a combined WRF and CityFFD method for calculating urban wind distributions. This study used WRF-CityFFD to calculate the wind distribution in the Kowloon district of Hong Kong within an area of 3.5 km × 2.4 km. Semi-empirical-CityFFD was also used for comparison. In addition, the applicability of the combined method was evaluated. Within the scope of this study, the following conclusions can be drawn:

- The WRF-CityFFD performed better than the semi-empirical-CityFFD in calculating wind velocities in urban microclimates.
- The power-law exponent for wind profiles should be carefully defined when conducting CFD simulations for complex urban layouts.
- Coastal areas with onshore wind conditions were recommended for selection as inflow boundary conditions for WRF-CityFFD.

Acknowledgments

This work was supported by Theme-based Research Scheme (Grant No. 22-504/21-R) from Research Grants Council of Hong Kong SAR, China, and the Research Institute for Sustainable Urban Development (RISUD). The authors would like to thank Dr. Mohammad Mortezazadeh and Mr. Jiwei Zou for their help in the use of the CityFFD.

References

[1] IPCC, Climate Change 2014 Synthesis Report, 2014.
[2] B. Blocken, J. Carmeliet, T. Stathopoulos, CFD evaluation of wind speed conditions in passages between parallel buildings—effect of wall-function roughness modifications for the atmospheric boundary layer flow, J. Wind Eng. Ind. Aerodyn. 95(9-11) (2007) 941-962.
[3] P. Moonen, T. Defraeye, V. Dorer, B. Blocken, J. Carmeliet, Urban Physics: Effect of the micro-climate on comfort, health and energy demand, Frontiers of Architectural Research 1(3) (2012) 197-228.
[4] B. Blocken, Computational Fluid Dynamics for urban physics: Importance, scales, possibilities, limitations and ten tips and tricks towards accurate and reliable simulations, Build. Environ. 91 (2015) 219-245.
[5] K.H. Schlünzen, D. Grawe, S.I. Bohnenstengel, I. Schlüter, R. Koppmann, Joint modelling of obstacle induced and mesoscale changes—Current limits and challenges, J. Wind Eng. Ind. Aerodyn. 99(4) (2011) 217-225.
[6] A. Mochida, I.Y.F. Lun, Prediction of wind environment and thermal comfort at pedestrian level in urban area, J. Wind Eng. Ind. Aerodyn. 96(10-11) (2008) 1498-1527.
[7] T. Stathopoulos, Pedestrian level winds and outdoor human comfort, J. Wind Eng. Ind. Aerodyn. 94(11) (2006) 769-780.
[8] B. Blocken, LES over RANS in building simulation for outdoor and indoor applications: A foregone conclusion?, Build. Simul. 11(5) (2018) 821-870.
[9] O. Palusci, P. Monti, C. Cecere, H. Montazeri, B. Blocken, Impact of morphological parameters on urban ventilation in compact cities: The case of the Tuscolano-Don Bosco district in Rome, Sci Total Environ 807(Pt 2) (2022) 150490.
[10] K. An, S.-M. Wong, J.C.-H. Fung, E. Ng, Revisit of prevailing practice guidelines and investigation of topographical treatment techniques in CFD-Based air ventilation assessments, Build. Environ. 169 (2020).
[11] N. Antoniou, H. Montazeri, H. Wigo, M.K.A. Neophytou, B. Blocken, M. Sandberg, CFD and wind-tunnel analysis of outdoor ventilation in a real compact heterogeneous urban area: Evaluation using “air delay”, Build. Environ. 126 (2017) 355-372.
[12] S. Liu, W. Pan, H. Zhang, X. Cheng, Z. Long, Q. Chen, CFD simulations of wind distribution in an urban community with a full-scale geometrical model, Build. Environ. 117 (2017) 11-23.
[13] S. Liu, W. Pan, X. Zhao, H. Zhang, X. Cheng, Z. Long, Q. Chen, Influence of surrounding buildings on wind flow around a building predicted by CFD simulations, Build. Environ. 140 (2018) 1-10.
[14] T. van Hooff, B. Blocken, Coupled urban wind flow and indoor natural ventilation modelling on a high-resolution grid: A case study for the Amsterdam ArenA stadium, Environ Modell Softw 25(1) (2010) 51-65.
[15] Y. Toparlar, B. Blocken, P. Vos, G.J.F. van Heijst, W.D. Janssen, T. van Hooff, H. Montazeri, H.J.P. Timmermans, CFD simulation and validation of urban microclimate: A case study for Bergpolder Zuid, Rotterdam, Build. Environ. 83 (2015) 79-90.
[16] M. Mortezazadeh, L. Wang, An adaptive time-stepping semi-Lagrangian method for incompressible flows, Numerical Heat Transfer, Part B: Fundamentals 75(1) (2019) 1-18.
[17] W. Zuo, Q. Chen, Improvements on the fast fluid dynamic model for indoor airflow simulation, Proceedings of SimBuild 4 (2010) 539-546.
[18] M. Mortezazadeh, L.L. Wang, M. Albettar, S. Yang, CityFFD – City fast fluid dynamics for urban microclimate simulations on graphics processing units, Urban Clim. 41 (2022) 101063.
[19] S. Zheng, Z.J. Zhai, Y. Wang, Y. Xue, L. Duanmu, W. Liu, Evaluation and comparison of various fast fluid dynamics modeling methods for predicting airflow around buildings, Build. Simul. 15(6) (2021) 1083-1095.
[20] M. Mortezazadeh, L.L. Wang, A high-order backward forward sweep interpolating algorithm for semi-Lagrangian method, Int. J. Numer. Methods Fluids 84(10) (2017) 584-597.

[21] T. Dai, S.M. Liu, J.J. Liu, N. Jiang, W. Liu, Q.Y. Chen, Evaluation of fast fluid dynamics with different turbulence models for predicting outdoor airflow and pollutant dispersion, Sustainable Cities and Society 77 (2022).
[22] M. Mortezazadeh, L. Wang, Solving city and building microclimates by fast fluid dynamics with large timesteps and coarse meshes, Build. Environ. 179 (2020).
[23] B. Blocken, T. Stathopoulos, J. Carmeliet, CFD simulation of the atmospheric boundary layer: wall function problems, Atmos Environ 41(2) (2007) 238-252.
[24] B. Blocken, A. van der Hout, J. Dekker, O. Weiler, CFD simulation of wind flow over natural complex terrain: Case study with validation by field measurements for Ria de Ferrol, Galicia, Spain, J Wind Eng Ind Aerod 147 (2015) 43-57.
[25] Tieleman, H. W. (2008). Strong wind observations in the atmospheric surface layer. Journal of wind engineering and industrial aerodynamics, 96(1), 41-77.
[26] Li, Q. S., Zhi, L., & Hu, F. (2010). Boundary layer wind structure from observations on a 325 m tower. Journal of wind engineering and industrial aerodynamics, 98(12), 818-832.
[27] Cook, N. J. (1997). The Deaves and Harris ABL model applied to heterogeneous terrain. Journal of wind engineering and industrial aerodynamics, 66(3), 197-214.
[28] A.I.o.J. (AIJ), AIJ Recommendations for Loads on Buildings, Japan, 2015.
[29] Y. Tominaga, A. Mochida, R. Yoshie, H. Kataoka, T. Nozu, M. Yoshikawa, T. Shirasawa, AIJ guidelines for practical applications of CFD to pedestrian wind environment around buildings, J. Wind Eng. Ind. Aerodyn. 96(10-11) (2008) 1749-1761.
[30] J. Wieringa, Updating the Davenport roughness classification, J. Wind Eng. Ind. Aerodyn. 41(1-3) (1992) 357-368.
[31] M. Huang, Z. Gao, S. Miao, F. Chen, M.A. LeMone, J. Li, F. Hu, L. Wang, Estimate of Boundary-Layer Depth Over Beijing, China, Using Doppler Lidar Data During SURF-2015, Boundary Layer Meteorol. 162(3) (2016) 503-522.
[32] M.M.F. Wong, J.C.H. Fung, J. Ching, P.P.S. Yeung, J.W.P. Tse, C. Ren, R. Wang, M. Cai, Evaluation of uWRF performance and modeling guidance based on WUDAPT and NUDAPT UCP datasets for Hong Kong, Urban Clim. 28 (2019).
[33] Y. He, C. Ren, H.W.L. Mak, C. Lin, Z. Wang, J.C.H. Fung, Y. Li, A.K.H. Lau, E. Ng, Investigations of high-density urban boundary layer under summer prevailing wind conditions with Doppler LiDAR: A case study in Hong Kong, Urban Clim. 38 (2021).
[34] C.H. Halios, J.F. Barlow, Observations of the Morning Development of the Urban Boundary Layer Over London, UK, Taken During the ACTUAL Project, Boundary Layer Meteorol 166(3) (2018) 395-422.
[35] J. Lim, Y. Akashi, R. Ooka, H. Kikumoto, Y. Choi, A probabilistic approach to the energy-saving potential of natural ventilation: Effect of approximation method for approaching wind velocity, Build. Environ. 122 (2017) 94-104.
[36] S. Du, X. Zhang, X. Jin, X. Zhou, X. Shi, A review of multi-scale modelling, assessment, and improvement methods of the urban thermal and wind environment, Build. Environ. 213 (2022).
[37] D.J. Gochis, J.L. Coen, D.O. Gill, J. Dudhia, C.A. Davis, W.C. Skamarock, J.B. Klemp, J.G. Powers, R. Ahmadov, S.E. Peckham, G.A. Grell, J. Michalakes, S. Trahan, S.G. Benjamin, C.R. Alexander, G.J. Dimego, W. Wang, C.S. Schwartz, G.S. Romine, Z. Liu, C. Snyder, F. Chen, M.J. Barlage, W. Yu, M.G. Duda, The Weather Research and Forecasting Model: Overview, System Efforts, and Future Directions, Bull. Am. Meteorol. Soc. 98(8) (2017) 1717-1737.
[38] K. Hammerberg, O. Brousse, A. Martilli, A. Mahdavi, Implications of employing detailed urban canopy parameters for mesoscale climate modelling: a comparison between WUDAPT and GIS databases over Vienna, Austria, Int. J. Climatol. 38 (2018) e1241-e1257.
[39] V. Masson, W. Heldens, E. Bocher, M. Bonhomme, B. Bucher, C. Burmeister, C. de Munck, T. Esch, J. Hidalgo, F. Kanani-Sühring, Y.-T. Kwok, A. Lemonsu, J.-P. Lévy, B. Maronga, D. Pavlik, G. Petit, L. See, R. Schoetter, N. Tornay, A. Votsis, J. Zeidler, City-descriptive input data for urban climate models: Model requirements, data sources and challenges, Urban Clim. 31 (2020).
[40] N.H. Wong, Y. He, N.S. Nguyen, S.V. Raghavan, M. Martin, D.J.C. Hii, Z. Yu, J. Deng, An integrated multiscale urban microclimate model for the urban thermal environment, Urban Clim. 35 (2021).

[41] M. Tewari, H. Kusaka, F. Chen, W.J. Coirier, S. Kim, A.A. Wyszogrodzki, T.T. Warner, Impact of coupling a microscale computational fluid dynamics model with a mesoscale model on urban scale contaminant transport and dispersion, Atmospheric Research 96(4) (2010) 656-664.
[42] M. Mortezazadeh, Z. Jandaghian, L.L. Wang, Integrating CityFFD and WRF for modeling urban microclimate under heatwaves, Sustainable Cities and Society 66 (2021).
[43] R.B. Li, Z.P. Liu, L. Feng, N.P. Gao, Fast fluid dynamics simulation of the airflow distributions in urban residential areas, Energy and Buildings 255 (2022).
[44] M. Mortezazadeh, L. Wang, SLAC – a semi-Lagrangian artificial compressibility solver for steady-state incompressible flows, International Journal of Numerical Methods for Heat & Fluid Flow 29(6) (2019) 1965-1983.
[45] J. Smagorinsky, General circulation experiments wiht the primitive equations I. The basic experiment, Monthly Weather Review 91(3) (1963) 99-164.
[46] Z. Jandaghian, H. Akbari, Effects of increasing surface reflectivity on aerosol, radiation, and cloud interactions in the urban atmosphere, Theor. Appl. Climatol. 139(3) (2020) 873-892.
[47] Z. Jandaghian, A.G. Touchaei, H. Akbari, Sensitivity analysis of physical parameterizations in WRF for urban climate simulations and heat island mitigation in Montreal, Urban Clim. 24 (2018) 577-599.
[48] NCEP GDAS/FNL 0.25 Degree Global Tropospheric Analyses and Forecast Grids, Research Data Archive at the National Center for Atmospheric Research, Computational and Information Systems Laboratory, Boulder, CO, 2015.
[49] M.B. Ek, K.E. Mitchell, Y. Lin, E. Rogers, P. Grunmann, V. Koren, G. Gayno, J.D. Tarpley, Implementation of Noah land surface model advances in the National Centers for Environmental Prediction operational mesoscale Eta model, J Geophys Res-Atmos 108(D22) (2003).
[50] F. Chen, H. Kusaka, R. Bornstein, J. Ching, C.S.B. Grimmond, S. Grossman-Clarke, T. Loridan, K.W. Manning, A. Martilli, S.G. Miao, D. Sailor, F.P. Salamanca, H. Taha, M. Tewari, X.M. Wang, A.A. Wyszogrodzki, C.L. Zhang, The integrated WRF/urban modelling system: development, evaluation, and applications to urban environmental problems, Int. J. Climatol. 31(2) (2011) 273-288.
[51] Z. Janjic, The step-mountain eta coordinate model: further developements of the convection, viscous sublayer, and turbulence closure schemes, Mon. Weather Rev. 122 (1994) 927-945.
[52] Y.-L. Lin, R.D. Farley, H.D. Orville, Bulk parameterization of the snow field in a cloud model, J. Appl. Meteorol. Climatol. 22(6) (1983) 1065-1092.
[53] G.A. Grell, D. Dévényi, A generalized approach to parameterizing convection combining ensemble and data assimilation techniques, Geophysical Research Letters 29 (2002) 1-38.
[54] M.J. Iacono, J.S. Delamere, E.J. Mlawer, M.W. Shephard, S.A. Clough, W.D. Collins, Radiative forcing by long-lived greenhouse gases: Calculations with the AER radiative transfer models, J. Geophys. Res.: Atmos. 113(D13) (2008).
[55] User's Guide for the Advanced Research WRF (ARW) Modeling System Version 4.0. https://www2.mmm.ucar.edu/wrf/users/docs/user_guide_v4/v4.0/contents.html.
[56] Y. Tominaga, R. Yoshie, A. Mochida, H. Kataoka, K. Harimoto, T. Nozu, Cross comparisons of CFD prediction for wind environment at pedestrian level around buildings, Part 2 (2005) 2661-2670.
[57] N. Luo, X. Luo, M. Mortezazadeh, M. Albettar, W.N. Zhang, D.X. Zhan, L. Wang, T.Z. Hong, A data schema for exchanging information between urban building energy models and urban microclimate models in coupled simulations, J Build Perform Simu (2022) 1-18.
[58] Hong Kong 2011 Population Census—Summary Results, Census and Statistics Department of Hong Kong, 2011.
[59] CADMAPPER. https://cadmapper.com/. (Accessed 3 March 2022).
[60] F. Jörg, B. Alexander, Best Practice Guideline for the CFD Simulation of Flows in the Urban Environment: COST Action 732 Quality Assurance and Improvement of Microscale Meteorological Models, COST Office: Brussels, Belgium (2007).
[61] G. Rosatti, R. Chemotti, L. Bonaventura, High order interpolation methods for semi-Lagrangian models of mobile-bed hydrodynamics on Cartesian grids with cut cells, Int. J. Numer. Methods Fluids 47 (2005) 1269-1275.
[62] K.-H. Kwak, S.-H. Lee, J.M. Seo, S.-B. Park, J.-J. Baik, Relationship between rooftop and on-road concentrations of traffic-related pollutants in a busy street canyon: Ambient wind effects, Environ. Pollut. 208 (2016) 185-197.

[63] Y. Gao, Z. Wang, C. Liu, Z.-R. Peng, Assessing neighborhood air pollution exposure and its relationship with the urban form, Build. Environ. 155 (2019) 15-24.